

Article

Analysis of Supersonic Flows inside a Steam Ejector with Liquid–Vapor Phase Change Using CFD Simulations

Hugues Charton, Christian Perret and Hai Trieu Phan *

CEA, Liten, Campus Ines, Université Grenoble Alpes, 73375 Le Bourget du Lac, France; hugues.charton2@cea.fr (H.C.); christian.perret@cea.fr (C.P.)

* Correspondence: haitrieu.phan@cea.fr

Abstract: In this work, different CFD models to compute flows inside a steam ejector were investigated. The results were compared to the analytical models as well as the experimental results from the literature. All the simulations gave realistic results from the hydrodynamic perspective with a relative error of the entrainment ratio between 25% and 40% compared to reference experimental data. However, an analysis of the temperature profiles showed that only realistic results from the thermodynamic perspective were given by multiphase calculations. The first multiphase model tested was the so-called Wet-Steam model from ANSYS Fluent. This model gave inconsistent results for the steam ejector CFD simulation due to the physical boundaries of this model. The second model tested was the Eulerian mixture model, which gave the most realistic results in terms of the physical conditions of the liquid and vapor phases inside the ejector. It also showed that the phase change could have a significant impact on the value of the critical output pressure as a way to improve the performance of the ejector.

Keywords: ejector; two-phase flows; CFD simulations



Citation: Charton, H.; Perret, C.; Phan, H.T. Analysis of Supersonic Flows inside a Steam Ejector with Liquid–Vapor Phase Change Using CFD Simulations. *Thermo* **2024**, *4*, 1–15. <https://doi.org/10.3390/thermo4010001>

Academic Editors: Emmanouil Rogdakis and George-Rafael Domenikos

Received: 24 November 2023

Revised: 9 January 2024

Accepted: 11 January 2024

Published: 12 January 2024



Copyright: © 2024 by the authors. Licensee MDPI, Basel, Switzerland. This article is an open access article distributed under the terms and conditions of the Creative Commons Attribution (CC BY) license (<https://creativecommons.org/licenses/by/4.0/>).

1. Introduction

In the current context of climate change and global warming, many new thermodynamic cycles have been developed and studied for the exploitation of low-grade heat sources (such as industrial waste heat or solar heat) to meet the growing need for refrigeration. Among the most studied low-grade heat-driven refrigeration cycles, i.e., absorption cycles [1], adsorption cycles [2], and ejector cycles [3], are gaining increasing attention.

The working principle of an ejector is described in detail by Meunier et al. [4]. A schematic representation of the ejector, as described by [5], is shown in Figure 1. The ejector operation is based on the use of a high-pressure primary fluid in order to draw in and drive a low-pressure secondary fluid. The primary fluid is fed through a convergent–divergent nozzle, which greatly increases its speed while greatly reducing its pressure. In the throat “t” of the nozzle, the primary fluid becomes sonic and is supersonic at the nozzle outlet. This high speed of the primary fluid causes a significant drop in the pressure in the mixing chamber; the latter becomes lower than the pressure of the secondary fluid. The secondary fluid is thereby sucked into the mixing chamber.

The primary and secondary fluids are considered perfectly mixed in the mixing section (section “y” in Figure 1), where the flow is supersonic. The fluid passes through the ejector’s throat at supersonic speed. Finally, within the diffuser, the flow reverts to subsonic velocity through a shock. In this way, the ejector diffuser induces an increase in the fluid pressure and a decrease in fluid velocity. To determine the ejector’s efficiency, it is useful to calculate the entrainment ratio ω , defined as the ratio of the secondary fluid mass flow to the primary fluid mass flow. The entrainment ratio can be plotted as a function of the ejector outlet pressure, as shown in Figure 2.

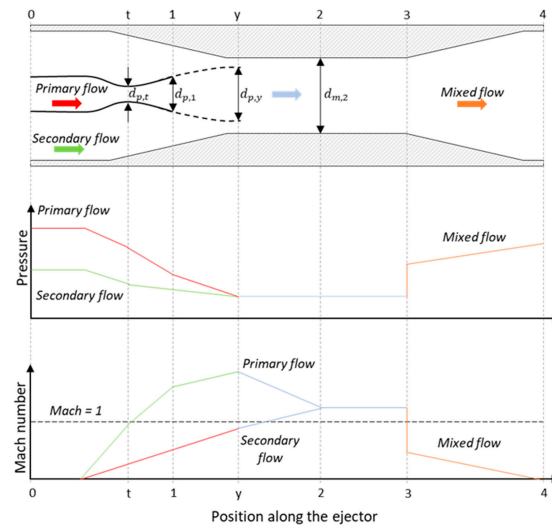


Figure 1. Schematic representation of the ejector according to [5].

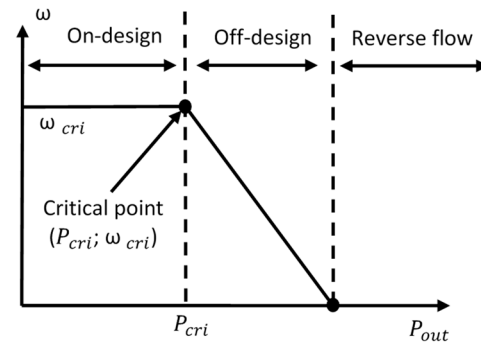


Figure 2. Ejector operating modes [5].

As illustrated in Figure 2, an ejector has three different operating modes. The first one, designated as “double choking”, corresponds to the nominal operating mode as described above. In this operating mode, the entrainment ratio ω remains constant as a function of the outlet pressure until it reaches a critical value P_{cri} . When $P_{out} > P_{cri}$, the ejector is no longer in the nominal operating range and two cases can be distinguished. In the first case, when the value of P_{out} is so high that it exceeds a second critical value called P_r , the flow is reversed. In this regime, the secondary fluid inlet has the lowest pressure point across the entire ejector. As a result, back flows occur, and both the primary fluid and ejector outlet fluid are drawn towards the secondary fluid inlet. In the second case, when $P_r > P_{out} > P_{cri}$, the flow is in the “single choking” mode. In this operating mode, only the primary fluid is drawn towards the outlet, and the entrainment ratio decreases sharply while increasing the outlet pressure.

In order to understand the local phenomena inside an ejector, several single-phase CFD 2D axisymmetric simulations, considering water (R718) vapor as an ideal gas, are available in the literature [6–8]. The results of these simulations were compared to the experimental test results by the same authors concerning the entrainment ratio. More specifically, in the case of Al-Doori (2013) [8], an experimental device for an ejector refrigeration cycle was fully set up, and several experiments measuring the pressure field along the ejector wall were carried out, with and without the observation of condensation phenomena. As far as the simulations were investigated, several turbulence models were implemented and tested. These simulations showed that modeling water vapor as an ideal gas without phase changes leads to significant discrepancies. In particular, Al-Doori (2013) found a critical pressure lower than experimental measurements and hypothesized that the absence of condensation modeling is responsible for this observation.

Simulations of 2D axisymmetric ejectors with phase change were carried out by Ariafiar et al. (2015) and Mazzelli et al. (2018) [9,10], with the so-called ANSYS Fluent “Wet-Steam” model and the $k-\omega$ SST turbulence model. For these simulations, Mazzelli et al. (2018) [10] implemented specific user-defined functions. These functions were directly developed by the users in order to overcome some limitations or restrictions of the models because the use of the ANSYS Fluent Wet-Steam model does not allow any change in parameters or settings. The results of these simulations were compared with experimental data from Al-Doori (2013) [8]. Ariafiar et al. (2015) [9] showed that the Wet-Steam model improved the modeling of physical phenomena compared to simulations carried out in single-phase ideal gas. In addition, Mazzelli et al. (2018) [10] showed that specific user-defined functions (condensation model, calculation of thermodynamic properties) allow an improvement in the accuracy of simulations.

Numerical studies carried out previously have shown the importance of accurately modeling the liquid–vapor phase changes in order to establish consistent and accurate numerical models for flow hydrodynamics within the ejector. However, these studies give little or no consideration to the temperature field distribution within the ejector. Mazzelli et al. (2018) [10] made one of the rare mentions of temperature fields and reported unrealistic calculated temperatures at the outlet of the primary fluid ejection nozzle. The researchers justify this result by pointing out that ice formation cannot be ruled out within an ejector. Ice formation was, in fact, observed by Al-doori (2013) [8].

However, for applications of ejectors in refrigeration cycles, it is necessary to have models that enable the prediction of both the hydrodynamic and the thermodynamic aspects of the flow. The main difficulty here is the huge pressure variation that happens inside an ejector, which leads to liquid–vapor phase change in highly compressible flows. The objective of this study is to investigate various modeling approaches and assess these models not only from hydrodynamics but also from a thermodynamics point of view. Three modeling approaches are investigated, all of which use the ANSYS Fluent simulation software as follows: the ideal gas simulation model, the homogeneous Eulerian model combined with the Lee condensation–evaporation mode, and the Wet-Steam model. To assess the different models, numerical results were compared to the experimental results of Ruangtrakoon et al. (2011) [11]. To the best of our knowledge, no experimental studies have implemented the measurement of temperature fields within an ejector. Therefore, only a physical analysis of the thermodynamic results obtained was proposed.

2. Model Description

2.1. Ideal Gas Model

In this model, the three Navier–Stokes Equations (1)–(3) were solved considering water vapor as an ideal gas. The RANS turbulence approach was used for turbulence modeling.

$$\frac{\partial \rho}{\partial t} + \nabla(\rho \vec{v}) = 0 \quad (1)$$

$$\frac{\partial \rho \vec{v}}{\partial t} + \nabla(\rho \vec{v} \vec{v}) = -\nabla P + \nabla \cdot (\bar{\tau}) + \rho \vec{g} \quad (2)$$

$$\frac{\partial}{\partial t} \left(\rho \left(E + \frac{v^2}{2} \right) \right) + \nabla \cdot \left(\rho v \left(h + \frac{v^2}{2} \right) \right) = \nabla \cdot \left(K_{eff} \nabla T + \nabla \tau_{eff} \vec{v} \right) \quad (3)$$

Here, ρ is the vapor density, \vec{v} is the vapor velocity, P is the pressure, τ is the viscous stress tensor, E is the total energy, h is enthalpy, and $K_{eff} = (K_l + K_t)$ is the heat transfer coefficient.

It was assumed that there was no phase change in the ejector. Two types of calculations were carried out under this assumption, using the $k-\omega$ SST turbulence model. The last

equation needed to close the system of equations was the equation of state. Here, it is the ideal gas law, Equation (4).

$$\frac{P}{\rho} = rT \quad (4)$$

where r is the ideal gas constant divided by the molar mass of water. The first calculation was performed using the ANSYS Fluent density solver and considering the steady-state flow. The second calculation was performed using the ANSYS Fluent pressure solver and using the pseudo-transient option.

2.2. Homogeneous Eulerian Model Combined with Lee Condensation–Evaporation Model

In the case of the homogeneous Eulerian model, also known as a one-fluid model or mixture model, a single fluid is considered, comprising the mixture of the vapor phase in which the liquid phase is assumed to be homogeneously dispersed. Navier–Stokes equations are solved for a single fluid called a mixture with velocity \vec{v}_m , density ρ_m , and viscosity η_m defined by Equations (5)–(7).

$$\vec{v}_m = \frac{\alpha_l \rho_l \vec{v}_l + \alpha_v \rho_v \vec{v}_v}{\rho_m} \quad (5)$$

$$\rho_m = \alpha_l \rho_l + \alpha_v \rho_v \quad (6)$$

$$\eta_m = \alpha_l \eta_l + \alpha_v \eta_v \quad (7)$$

where the index l is the liquid, the index v is the vapor, α_l is the volume fraction of liquid water, and α_v is volume fraction of water vapor.

These quantities can then be used to solve the Navier–Stokes Equations (8)–(10).

$$\frac{\partial \rho_m}{\partial t} + \nabla \cdot (\rho_m \vec{v}_m) = 0 \quad (8)$$

$$\frac{\partial \rho_m \vec{v}_m}{\partial t} + \nabla \cdot (\rho_m \vec{v}_m \vec{v}_m) = -\nabla P + \nabla \cdot \left(\mu_m \left(\nabla \vec{v}_m + \nabla \vec{v}_m^T \right) \right) - \nabla \cdot (\alpha_l \rho_l \vec{v}_{dr,l} \vec{v}_{dr,l}) \quad (9)$$

$$\frac{\partial}{\partial t} (\alpha_l \rho_l E_l + \alpha_v \rho_v E_v) + \nabla \cdot (\alpha_l \vec{v}_l (\rho_l E_l + P) + \alpha_v \vec{v}_v (\rho_v E_v + P)) = \nabla \cdot (K_{eff} \nabla T_m + \nabla \tau_{eff,v} \vec{v}_m) \quad (10)$$

Here, $E_i = h_i - \frac{P}{\rho_i} + \frac{v_m^2}{2}$; $K_{eff} = \alpha_l (K_l + K_t) + \alpha_v (K_v + K_t)$ is the heat transfer coefficient; $\vec{v}_{dr,l} = \vec{v}_l - \vec{v}_m$ is the drift velocity of the liquid phase.

The drift velocity of the liquid phase is derived from the relative velocity $\vec{v}_{r,lv} = \vec{v}_v - \vec{v}_l$ using Equation (11).

$$\vec{v}_{dr,l} = \vec{v}_{r,lv} - \frac{\alpha_l \rho_l}{\rho_m} \vec{v}_{r,lv} \quad (11)$$

$\vec{v}_{r,lv}$ is determined using Equations (12)–(14).

$$\vec{v}_{r,lv} = \frac{\tau_p}{f_{drag}} \frac{\rho_l - \rho_m}{\rho_l} \vec{a} \quad (12)$$

where \vec{a} is the droplet acceleration and τ_p is the particle relaxation time.

$$\tau_p = \frac{\rho_l D_{\delta}^2}{18 \mu_v} \quad (13)$$

$$f_{drag} = \begin{cases} 1 + 0.15 Re^{0.687} & \text{si } Re < 1000 \\ 0.01 Re & \text{si } Re > 1000 \end{cases} \quad (14)$$

In addition to these equations, the volume fraction of the liquid phase is determined using Equation (15).

$$\frac{\partial \alpha_l \rho_l}{\partial t} + \nabla \cdot (\alpha_l \rho_l \vec{v}_m) = -\nabla \cdot (\alpha_l \rho_l \vec{v}_{dr,l}) + \dot{m}_{l \rightarrow v} - \dot{m}_{v \rightarrow l} \quad (15)$$

where $\dot{m}_{v \rightarrow l}$ is the evaporation mass flow rate and $\dot{m}_{l \rightarrow v}$ is the condensation mass flow rate. The Lee evaporation and condensation model, based on the work of Lee (1979) [12], is available in Fluent. It allows the calculation of evaporation and condensation rates using Formulas (16) and (17).

In the cells where $T_l > T_{sat}$:

$$\dot{m}_{l \rightarrow v} = C_1 \alpha_l \rho_l \frac{(T_l - T_{sat})}{T_{sat}} \quad (16)$$

In the cells where $T_v < T_{sat}$:

$$\dot{m}_{v \rightarrow l} = C_2 \alpha_v \rho_v \frac{(T_{sat} - T_v)}{T_{sat}} \quad (17)$$

Here, C_1 and C_2 are the coefficients to be calibrated using the experimental results or other simulations. The recommended values for these coefficients are between 0.1 and 1000 Hz. However, it is possible to use much higher values at the risk of achieving a less converged calculation.

Tables of values for the thermodynamic properties of gases and liquids were generated using ANSYS Fluent to close the system of equations with an equation of state. The use of this kind of table is supposed to be better adapted than the ideal gas law. Indeed, the flow reaches a high Mach number, hence showing that it is highly compressible. These RGP (Real Gas Property) tables are generated using the NIST (National Institute of Standards and Technology) polynomials and the REFPROP database.

2.3. Wet-Steam Model

Fluent's Wet Steam model is also a homogeneous Eulerian model. It is initially based on Equations (2)–(12). However, the phase change model relies on the nucleation theory to calculate condensation and evaporation mass flow rates.

The Wet-Steam model assumes that the relative velocity between the droplets and the gas phase is negligible, as are the interactions between the droplets (coalescence and break-up). The model assumes that the liquid mass fraction β remains below 0.1 and the droplet size is very small so that the volume of the liquid phase can be neglected. In this way, the model uses two transport equations, one for the liquid mass fraction β (18) and one for the number of droplets per unit volume n Equation (19).

$$\frac{\partial \rho \beta}{\partial t} + \nabla \cdot (\rho v \beta) = R \quad (18)$$

$$\frac{\partial \rho n}{\partial t} + \nabla \cdot (\rho v n) = \rho I \quad (19)$$

The model defines the mixture density differently than Equation (6), simply from Equation (20).

$$\rho = \frac{\rho_v}{(1 - \beta)} \quad (20)$$

where R is the mass generation rate in $\text{kg}/(\text{m}^3 \cdot \text{s})$ due to evaporation and condensation, and I is the nucleation rate (the number of new drops per unit volume per second).

Fluent uses various relations and change-of-state laws to calculate the source terms R and I in Equations (18) and (19). Equation (21) derives R from I .

$$R = \frac{4}{3} \pi \rho_l r_*^3 I \quad (21)$$

Here, r_* is the Kelvin–Helmholtz critical radius, such that $r > r_*$ implies that the drop will grow and $r < r_*$ implies that the drop evaporates. This radius is itself given by Formula (22), which involves σ as the surface tension.

$$r_* = \frac{2\sigma}{\rho_l RT \ln\left(\frac{P}{P_{sat}(T)}\right)} \quad (22)$$

Finally, I is calculated using Equation (23), which describes the classical theory of nucleation.

$$I = \frac{q_c}{(1 + \theta)} * \left(\frac{\rho_v^2}{\rho_l}\right) * \sqrt{\frac{2\sigma}{m_{molecule}^3 * \pi}} * \exp\left(-\left(\frac{4\pi r_*^2 \sigma}{3k_B T}\right)\right) \quad (23)$$

where $m_{molecule}$ is the mass of a molecule, q_c is an evaporation coefficient, k_B is Boltzmann's constant, θ and is a correction factor for the non-isothermal nature of the phenomenon, calculated using Equation (24).

$$\theta = \frac{2(\gamma - 1)}{\gamma + 1} * \left(\frac{h_{lv}}{RT}\right) * \left(\frac{h_{lv}}{RT} - 0.5\right) \quad (24)$$

In the case of the Wet-Steam model, the equation of state is a rather complex, real gas equation specially designed to solve wet-steam problems. This law is given using Equation (25).

$$P = \rho_v RT \left(1 + B\rho_v + C\rho_v^2 + D\rho_v^3\right) \quad (25)$$

The values of B, C, and D are given using Equations (26)–(28).

$$B = -\frac{e}{GT} - \varphi_1 + b \quad (26)$$

$$C = -b\varphi_1 + 4\varphi_1^2\varphi_2 \quad (27)$$

$$D = 32b\varphi_1^2\varphi_2 \quad (28)$$

where $e = 63.2$, $b = 0.00085$, $\varphi_1 = \frac{EG}{TW_1}$, $\varphi_2 = 1 - \frac{K}{TW_2}$, $E = 0.39 * 10^6$, $G = 47.053$, $K = 22.7$, $n = 0.355/10^7$, $m_1 = 1.968$, $m_2 = 2.957$, $W_1 = \frac{3+2m_1}{2}$, and $W_2 = \frac{3m_2-4m_1}{2}$.

This model can also be used to calculate certain thermodynamic properties of the fluid. According to the ANSYS Fluent guide, the specific enthalpy of steam is given in Equation (29), and the entropy can be calculated using Formula (30).

$$h_v = \frac{P}{\rho_v} - RT^2 \left(\frac{dB}{dT}\rho_v + \frac{1}{2}\frac{dC}{dT}\rho_v^2 + \frac{1}{3}\rho_v^3\right) + 10^3 \left(1.111177T + 3.55878/10^4 T^2 - \frac{6991.96}{T} + 2070.54\right) \quad (29)$$

$$s_v = R \left(\ln\left(\frac{1}{\rho_v}\right) - B\rho_v - \frac{1}{2}C\rho_v^2 - \frac{1}{3}D\rho_v^3\right) - RT \left(\frac{dB}{dT}\rho_v + \frac{1}{2}\frac{dC}{dT}\rho_v^2 + \frac{1}{3}\rho_v^3\right) + 10^3 \left(1.111177\ln(T) + 7.11756/10^4 T^2 - 3495.98T^2 + 0.30773\right) \quad (30)$$

The heat capacities of steam at constant pressure and constant volumes are given using Equations (31) and (32).

$$CV_v = \frac{\partial}{\partial T} \left(h_v - \frac{P}{\rho_v}\right) \quad (31)$$

$$CP_v = CV_v + \frac{\rho_v^2 T \left(\frac{\partial P}{\partial T} \right)^2}{\frac{\partial P}{\partial \rho_v}} \quad (32)$$

3. Methods Section

3.1. Ejector Geometry

As mentioned previously, in this work, the experimental results obtained by Ruangtrakoon et al. (2011) [11] were used as a study case to assess the modeling and simulation results. The ejector geometry reproduced here is one of the geometries used by Ruangtrakoon et al. (2011) [11], and its main characteristics are shown in Table 1.

Table 1. Characteristics of the modeled ejector from the geometry of [11].

	Mixing Chamber	Ejector Throat	Diffuser	Secondary Fluid Inlet	Primary Fluid Nozzle
Length (mm)	130	114	180	44	67
Maximum diameter (mm)	24	19 (constant)	40	46.6	7.75

As for the primary fluid inlet nozzle, the fluid enters a 7.5 mm diameter tube, then passes through a convergent nozzle with a 1.4 mm diameter throat before passing through a divergent nozzle with a 10° opening angle. With this geometry, the ejector drive ratio was determined by varying the outlet pressure. The results are shown in Figure 3, which gives the ejector entrainment ratio as a function of the ejector outlet pressure.

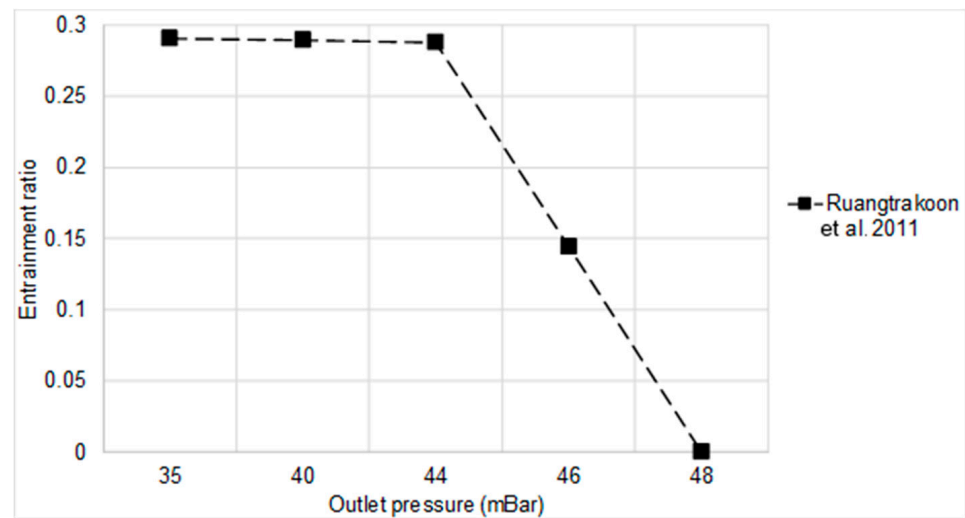


Figure 3. Experimental results for the chosen conditions from Ruangtrakoon et al. (2011) [11].

3.2. Meshing and Boundary Conditions

The ejector geometry was reproduced using the ANSYS Design Modeler software, and a mesh was constructed using Ansys Meshing. This mesh is shown in Figures 4–6.

The mesh is made of 26,000 cells. Only half the geometry was modeled, and an axisymmetry condition was used on the central axis of the ejector. The y^+ of the mesh was between 1 and 10 on the outer wall and between 1 and 120 on the inner wall. The flow boundary conditions associated with the various mesh boundaries are presented in Table 2.

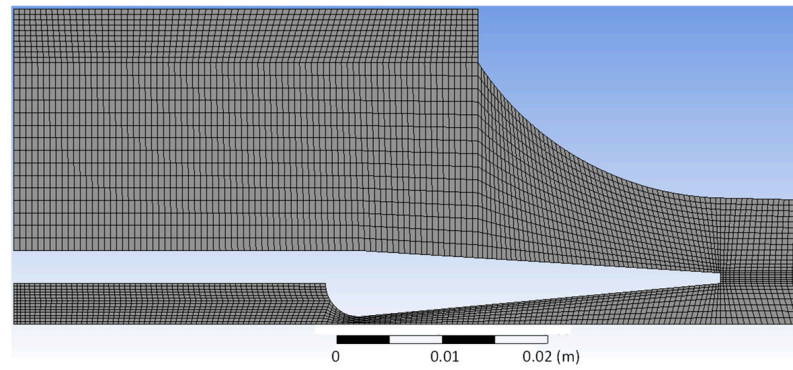


Figure 4. Mesh of the ejector inlets.

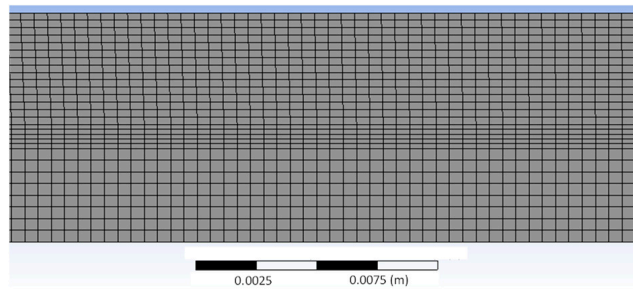


Figure 5. Mesh of the ejector throat.

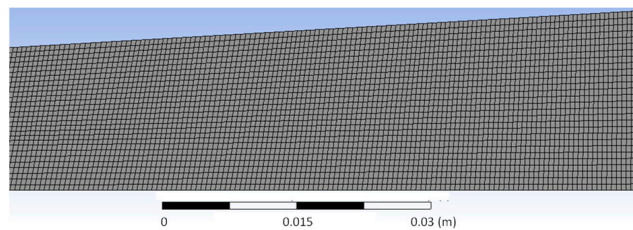


Figure 6. Mesh of the ejector divergent.

Table 2. Boundary conditions of the flow inside the ejector.

	Primary Fluid Inlet	Secondary Fluid Inlet	Outlet
Type of boundary condition	Pressure inlet	Pressure inlet	Pressure outlet
Pressure (Pa)	476,160	1037	3000
Temperature (°C)	150	7.5	

The pressure boundary conditions for the inlets listed in Table 2 correspond to the saturation pressures associated with the fluid inlet temperatures.

To check the influence of the mesh size, a mesh twice as refined was created in order to compare the results obtained for the same simulation with two different meshes. For this, simulations with each mesh were launched using the single-phase ideal gas model. The Mach numbers were extracted and plotted along the centerline of the ejector. The results are shown in Figure 7.

Figure 7 shows that the results are nearly identical. The mesh refinement level had no impact on the calculation results.

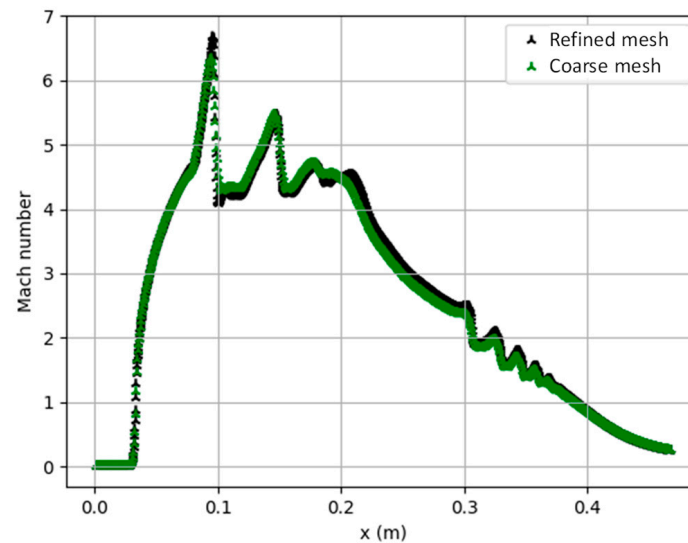


Figure 7. Evolution of the Mach number along the middle ejector axis.

3.3. Calibration of the Coefficients of the Homogeneous Eulerian Model Combined with Lee Condensation–Evaporation Model

With ANSYS Fluent, in order to use the homogeneous Eulerian model combined with the Lee condensation–evaporation model, it was necessary to calibrate the coefficients C_1 and C_2 . First, an analysis of the impact of these coefficients on the calculation results was carried out on a nozzle calculation case. It was found that these coefficients have no impact on the flow pressure and velocity fields. However, these coefficients do have a significant impact on the calculation of the liquid mass fraction and temperature fields. In the case of the ejector calculation, the coefficients were calibrated in order to maintain good calculation convergence while keeping the minimum temperature as high as possible and the amount of superheated liquid as low as possible. Indeed, the minimum temperature should not be very low compared to the melting point temperature ($0\text{ }^\circ\text{C}$ for water) in order to avoid crystallization that blocks the operation of the ejector. Both coefficients were, therefore, set at a value of 300,000 Hz.

4. Results and Discussion

In order to analyze the simulation results, the fields of pressure, Mach number, temperature, and mass fraction were extracted and plotted along the centerline of the ejector.

4.1. Temperature Analysis of the Single-Phase Ideal Gas Model

In Figure 8, the pressure, Mach number, and temperature fields along the red line of the ejector are plotted. Figure 8 shows how flow temperature varies in a similar way to the pressure. Thus, when using a single-phase model, pressure and temperature variations are closely linked. The temperature is the highest at the inlet of the primary fluid nozzle, then drops as the fluid expands through the throat. The temperature is then minimal in low-pressure zones and increases with pressure. The minimum temperature reached here is $-212\text{ }^\circ\text{C}$, and values below $0\text{ }^\circ\text{C}$ are reached over a significant proportion of the ejector. Although negative values may be realistic, values so close to absolute zero cannot be considered consistent. This is a clear limitation of this model, which does not take condensation into account, whereas it has been observed experimentally.

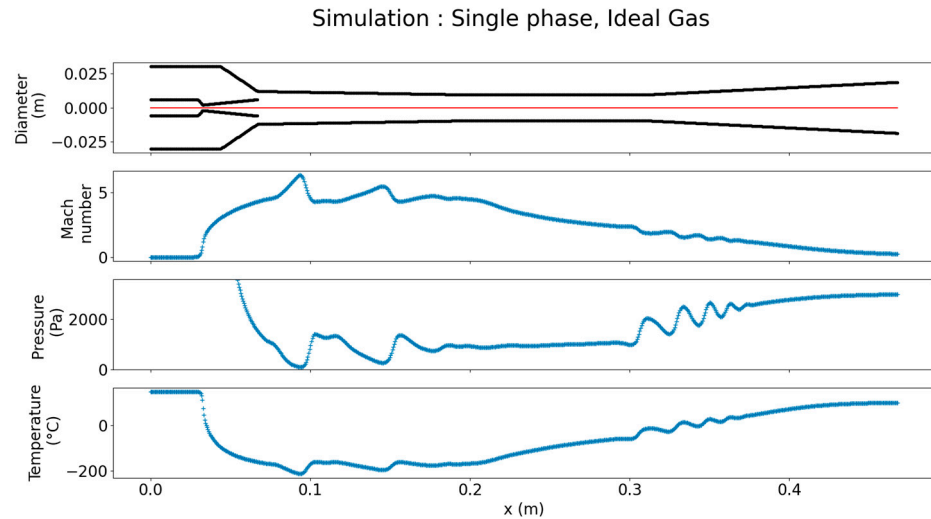


Figure 8. Simulation results for the single-phase model, ideal gas, and density solver.

4.2. Temperature Analysis of the Wet-Steam Model

An analysis of the temperature field shows that the minimum temperature reached within the ejector was $-163\text{ }^{\circ}\text{C}$. This value can be seen in Figure 9, which plots the pressure, Mach number, temperature, and liquid mass fraction fields along the red line of the ejector.

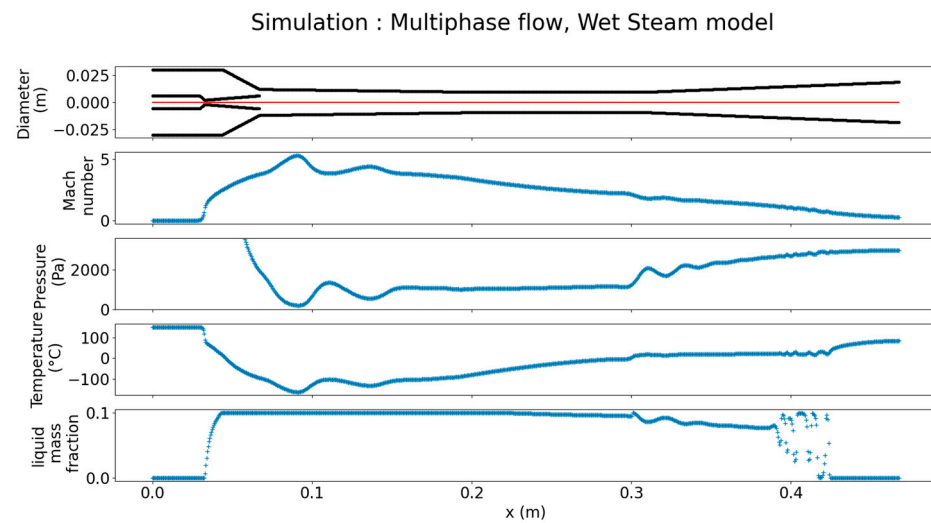


Figure 9. Simulation results using the Wet-Steam model and density solver.

Figure 9 shows that temperature variations are once again closely linked to pressure variations within the ejector. The minimum temperature this time is $-163\text{ }^{\circ}\text{C}$. This value is higher than the minimum value reached in the ideal gas simulation but remains too far below $0\text{ }^{\circ}\text{C}$. The calculated temperatures within the ejector are, therefore, better than the single-phase simulation but still not physically consistent. An analysis of the liquid mass fraction field provides an initial explanation for the failure of the Wet-Steam model. It appears that the liquid mass fraction is initially zero in the primary fluid nozzle, then rises sharply at the nozzle's throat. Downstream of the nozzle throat, the liquid mass fraction limit of 0.1 imposed by the model is reached on many cells. Finally, the liquid water mass fraction oscillates and then decreases in the divergent ejector. The fact that the mass fraction reaches the 0.1 limit indicates that condensation is limited when using this model. Limited condensation means that the latent heat released during condensation is underestimated in the calculation, thus explaining the low temperatures calculated when using ANSYS Fluent.

In addition to checking that the condensation phenomenon has been correctly modeled, it is important to check that the evaporation phenomenon has also been correctly modeled. To check this, it is necessary to ensure that the calculation does not generate superheated liquid water. To this end, a surface was created in ANSYS Fluent, containing only meshes with more than 5% liquid water by mass. The temperature field on this surface is shown in Figure 10.

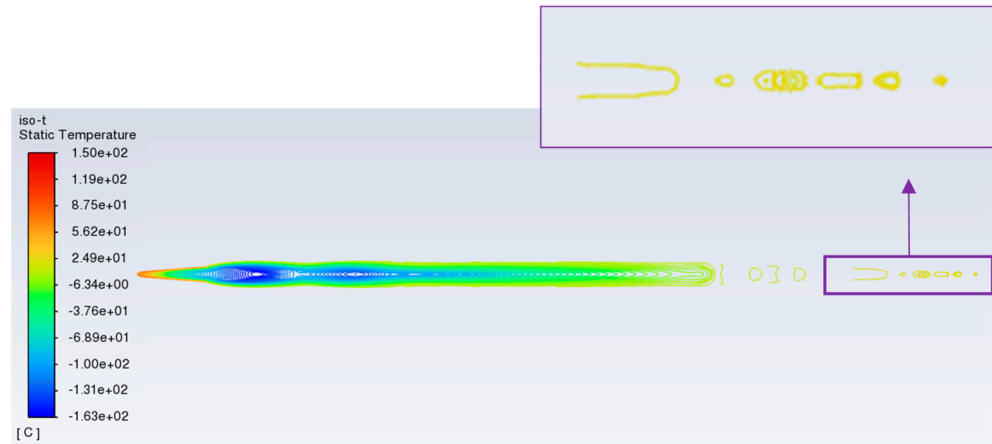


Figure 10. Temperature of areas with at least 5% liquid water and the Wet-Steam model.

Figure 10 shows that the temperature only exceeds 100 °C on a very small number of meshes containing more than 5% liquid water. As a result, the calculation results show very little superheated liquid. The Wet-Steam model, therefore, shows no problem in modeling the evaporation phenomenon.

4.3. Temperature Analysis of the Homogeneous Eulerian Model Combined with Lee Condensation–Evaporation Model

An analysis of the temperature field showed that the minimum temperature reached within the ejector was $-14\text{ }^{\circ}\text{C}$. This value can be seen in Figure 11, which plots the pressure, Mach number, temperature, and liquid mass fraction fields along the red line of the ejector.

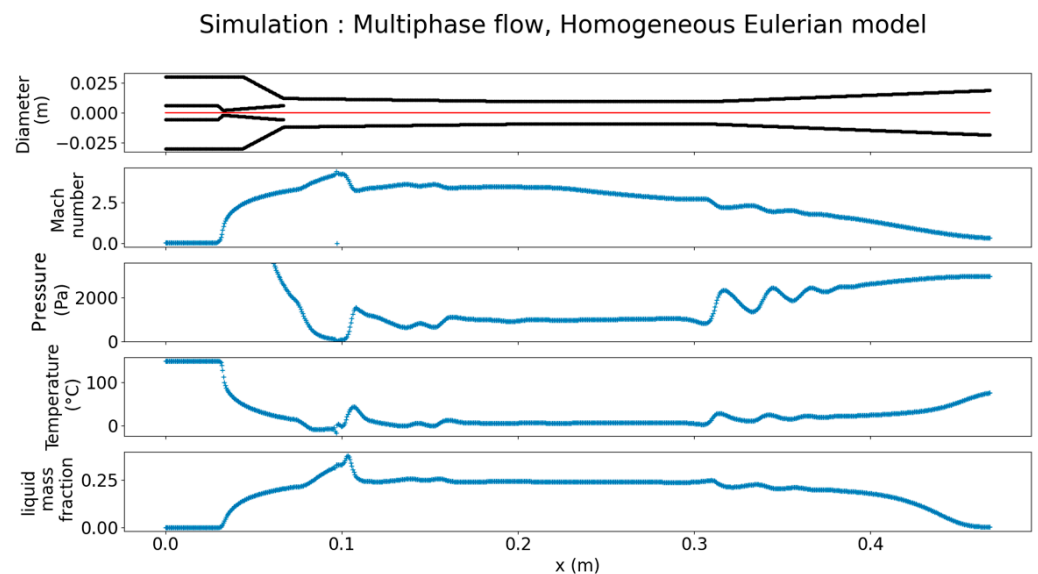


Figure 11. Simulation results using the homogeneous Eulerian model and pressure solver.

Similar to the two previous simulations, Figure 11 shows that pressure variations are always closely linked to the temperature field calculation. The minimum temperature

reached is $-14\text{ }^{\circ}\text{C}$, which is a much more plausible value when compared with the results of the other models. Indeed, although this value is negative, the presence of a potential liquid water solidification phenomenon cannot be ruled out. Thus, the absence of solidification and melting modeling in the calculation may explain the minimum temperature of $-14\text{ }^{\circ}\text{C}$. An analysis of the liquid water mass fraction field helps to better explain this result. Here, the liquid mass fraction rises from the nozzle throat until it reaches a maximum value of 0.37 in the mixing chamber. The mass fraction then stagnates at a value of around 0.25 until it reaches the ejector divergent, where it decreases to almost zero at the outlet. Thus, the absence of a limitation in terms of water vapor condensation is the key point that enabled the calculation to reach plausible temperature values. It is important to make the same analysis for the Wet-Steam model with regard to the possibility of superheated liquid within the ejector.

Applying the same approach to the Wet-Steam model results, it is possible to observe the temperature for ejector zones containing 5% or more liquid water. The results are shown in Figure 12.

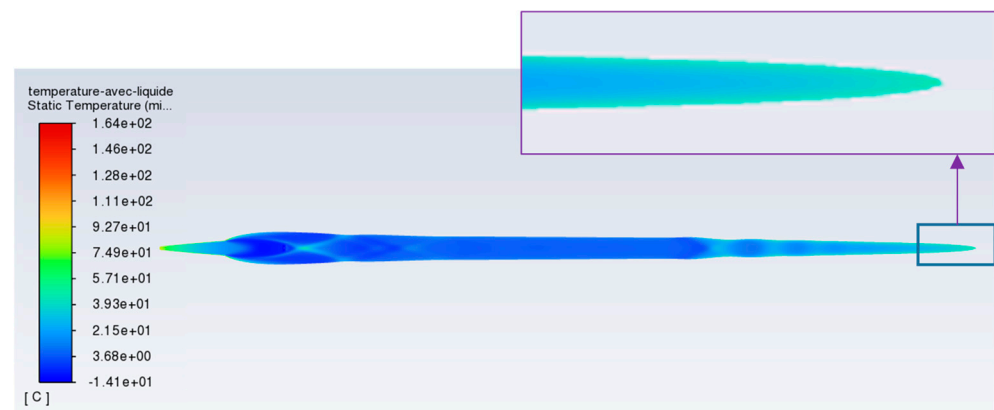


Figure 12. Temperature in areas with at least 5% liquid water for the homogeneous Eulerian model.

Figure 12 shows the same conclusions as the Wet-Steam model as follows: the temperature only exceeds $100\text{ }^{\circ}\text{C}$ on a very small number of meshes containing more than 5% liquid water. As a result, the calculation results show very little superheated liquid. Therefore, the homogeneous Eulerian model shows no problem here in modeling the evaporation phenomenon. Hence, the homogeneous Eulerian model gives realistic and consistent results from both hydrodynamic and thermodynamic points of view. This new model achieves an entrainment ratio value of 0.398, compared with 0.394 for the single-phase ideal gas simulation and the pressure solver. Thus, the addition of phase change is, above all, an improvement in the ability to predict thermodynamic phenomena within the flow.

4.4. Comparison of Simulation Entrainment Ratio

After each simulation, the mass flow rates of the primary and secondary fluids were extracted to evaluate the ejector entrainment ratio. The results are given in Table 3.

Table 3. Comparison of entrainment ratios obtained with the different models tested.

	Single Phase Ideal Gas Model	Single Phase Ideal Gas Model	Wet-Steam Model	Homogeneous Eulerian Model
Solver used	Density-based	Pressure-based	Density-based	Pressure-based
ω	0.463	0.394	0.456	0.398
Relative error with experience (%)	37.6	26.6	36.6	27.3

It was observed that the order of magnitude for all the models was in good agreement with the experimental results, but a more accurate prediction of the entrainment ratio was obtained with the pressure-based solver. In order to determine the critical pressures, several simulations were carried out by varying the output pressure for the two simulation cases, which gave the best results.

Figure 13 shows that the homogeneous Eulerian model predicts a higher value of the critical output pressure compared to the ideal gas model. This means that the change in the liquid–vapor phase could have a significant impact on the performance of the ejector. Further experimental works are necessary in order to validate this numerical observation.

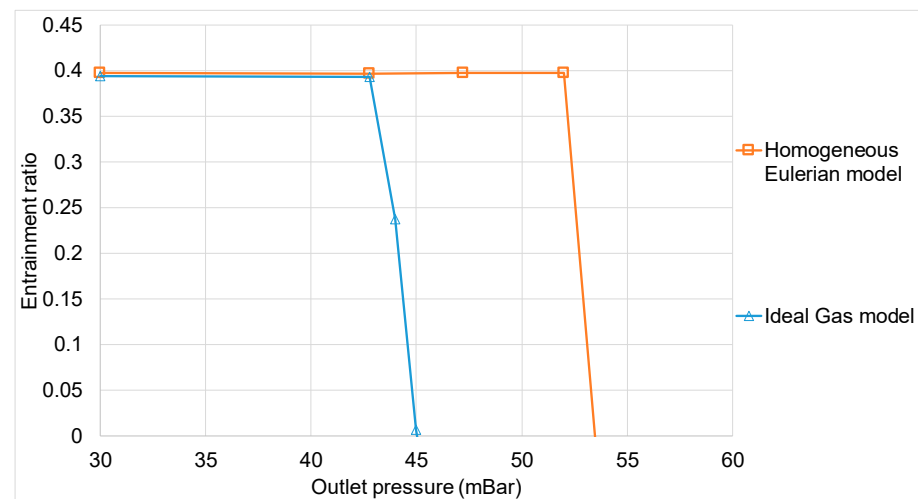


Figure 13. Entrainment ratio calculated as a function of output pressure.

5. Conclusions

In this work, three different flow models were tested to simulate the flow of water vapor through an ejector designed for a cold production cycle. The hydrodynamic results of the calculations were compared to the experimental results in the literature. The thermodynamic results of the calculations were physically analyzed but could not be compared with reality. The first of the three models was a single-phase model that did not take phase changes into account. This model did not give physically consistent results from a thermodynamic point of view. The second model was the ANSYS Fluent Wet-Steam model. This model took into account liquid–vapor phase change phenomena up to a certain liquid mass fraction limit. As this limit needed to be exceeded, the results were still not consistent from a thermodynamic point of view. Finally, the last model was a homogeneous Eulerian model coupled with the Lee model of evaporation and condensation and RGP tables for thermodynamic property calculations. This model was found to give plausible thermodynamic results. In particular, it was observed that the liquid–vapor phase change inside the ejector could have a significant impact on the value of the critical outlet pressure. Further experimental works are needed in order to validate this observation as well as the evolution of the fluid temperature profiles.

Author Contributions: Writing—original draft, H.C.; Writing—review & editing, C.P. and H.T.P. All authors have read and agreed to the published version of the manuscript.

Funding: This research was funded by the French Alternative Energies and Atomic Energy Commission.

Conflicts of Interest: The authors declare no conflicts of interest.

Nomenclature

Common letters:

P	Pressure	Pa
T	Temperature	K
M	Mach number	-
D	Diameter	m
\dot{m}_p	Mass flow rate of the primary fluid	kg/s
\dot{m}_s	Mass flow rate of the secondary fluid	kg/s
h	Enthalpy	J
k	Turbulent kinetic energy	m^2/s^2
v	Velocity	m/s
K	Heat transfer coefficient	$\text{W}/\text{m}^2/\text{K}$
K_t	Turbulent heat transfer coefficient	$\text{W}/\text{m}^2/\text{K}$
f_{drag}	Drag force	N
$\dot{m}_{l \rightarrow v}$	Evaporation mass flow rate	kg/s
$\dot{m}_{v \rightarrow l}$	Condensation mass flow rate	kg/s
v_{dr}	Drift velocity	m/s
C	Lee model coefficient	Hz
n	Number of droplets per unit volume	m^{-3}
R	Mass generation rate due to evaporation and condensation	$\text{kg}/(\text{m}^3 \cdot \text{s})$
I	Nucleation rate	m^{-3}/s
r_*	Kelvin–Helmholtz critical radius	m
$m_{molecule}$	Mass of single molecule	kg
k_B	Boltzmann constant	$\text{m}^2\text{kg}/(\text{s}^2\text{K})$
r	Ideal gas constant divided by molar mass	$\text{J}/(\text{K} \cdot \text{kg})$
E	Total energy	J
Pr_t	Turbulent Prandtl number	-
Re	Reynold number	-
C_p	The heat capacities at constant pressure	J/K
C_v	The heat capacities at constant volume	J/K

Greek letters:

ρ	Density	kg/m^3
ω	Entrainment ratio	-
ε	Turbulent dissipation rate	m^2/s^3
η	Dynamic viscosity	Pa.s
μ	Kinematic viscosity	m^2/s
η_t	Turbulent viscosity	Pa.s
τ_p	Particles relaxation time	s
β	Liquid mass fraction	-
σ	Surface tension	N/m
θ	Correction factor	-
γ	Laplace coefficient	-
α_i	Volume fraction of phase i	-
τ	Viscous stress tensor	Pa

Index:

c	critical
r	reverse
m	mixture
l	liquid
v	vapor
sat	saturation

References

1. Voeltzel, V.; Phan, H.T.; Blondel, Q.; Gonzalez, B.; Tauveron, N. Steady and dynamical analysis of a combined cooling and power cycle. *Therm. Sci. Eng. Prog.* **2020**, *19*, 100650. [[CrossRef](#)]
2. Godefroy, A.; Perier-Muzet, M.; Mazet, N. Thermodynamic analyses on hybrid sorption cycles for low-grade heat storage and cogeneration of power and refrigeration. *Appl. Energy* **2019**, *255*, 113751. [[CrossRef](#)]

3. Elbel, S.; Lawrence, N. Review of recent developments in advanced ejector technology. *Int. J. Refrig.* **2016**, *62*, 1–18. [[CrossRef](#)]
4. Meunier, F.; Neveu, P. Convertisseurs thermiques—Machines frigorifiques. Pompes à chaleur. Thermotransformateurs. *Froid Ind.* **2018**, *BE 9 734v2*, 1–17. [[CrossRef](#)]
5. Braccio, S.; Guillou, N.; Le Pierrès, N.; Tauveron, N.; Phan, H.T. Mass-Flowrate-Maximization Thermodynamic Model and Simulation of Supersonic Real-Gas Ejectors Used in Refrigeration Systems. *Therm. Sci. Eng. Prog.* **2023**, *37*, 101615. [[CrossRef](#)]
6. Ruangtrakoon, N.; Thongtip, T.; Aphornratana, S.; Sriveerakul, T. CFD Simulation on the Effect of Primary Nozzle Geometries for a Steam Ejector in Refrigeration Cycle. *Int. J. Therm. Sci.* **2013**, *63*, 133–145. [[CrossRef](#)]
7. Bumrunghthaichaichan, E.; Ruangtrakoon, N.; Thongtip, T. Performance Investigation for CRMC and CPM Ejectors Applied in Refrigeration under Equivalent Ejector Geometry by CFD Simulation. *Energy Rep.* **2022**, *8*, 12598–12617. [[CrossRef](#)]
8. Al-Doori, G. Investigation of Refrigeration System Steam Ejector Performance through Experiments and Computational Simulations. Ph.D. Thesis, University of Queensland, Brisbane, Australia, 2013.
9. Ariaifar, K.; Buttsworth, D.; Al-Doori, G.; Malpress, R. Effect of Mixing on the Performance of Wet Steam Ejectors. *Energy* **2015**, *93*, 2030–2041. [[CrossRef](#)]
10. Mazzelli, F.; Giacomelli, F.; Milazzo, A. CFD Modeling of Condensing Steam Ejectors: Comparison with an Experimental Test-Case. *Int. J. Therm. Sci.* **2018**, *127*, 7–18. [[CrossRef](#)]
11. Ruangtrakoon, N.; Aphornratana, S.; Sriveerakul, T. Experimental Studies of a Steam Jet Refrigeration Cycle: Effect of the Primary Nozzle Geometries to System Performance. *Exp. Therm. Fluid Sci.* **2011**, *35*, 676–683. [[CrossRef](#)]
12. Lee, W.H. *A Pressure Iteration Scheme for Two-Phase Modeling*; Technical Report LA-UR 79-975; Los Alamos Scientific Laboratory: Los Alamos, NM, USA, 1979.

Disclaimer/Publisher’s Note: The statements, opinions and data contained in all publications are solely those of the individual author(s) and contributor(s) and not of MDPI and/or the editor(s). MDPI and/or the editor(s) disclaim responsibility for any injury to people or property resulting from any ideas, methods, instructions or products referred to in the content.